THE JOURNAL OF BIOLOGICAL CHEMISTRY VOL. 291, NO. 24, pp. 12838–12850, June 10, 2016

Heterogeneity in the Histidine-brace Copper Coordination Sphere in Auxiliary Activity Family 10 (AA10) Lytic Polysaccharide Monooxygenases*

Received for publication, February 17, 2016, and in revised form, April 5, 2016 Published, JBC Papers in Press, April 15, 2016, DOI 10.1074/jbc.M116.722447

Amanda K. Chaplin[‡1], Michael T. Wilson[‡], Michael A. Hough[‡], Dimitri A. Svistunenko[‡], Glyn R. Hemsworth[§], Paul H. Walton[§], Erik Vijgenboom[¶], and Jonathan A. R. Worrall[‡2]

From the [‡]School of Biological Sciences, University of Essex, Wivenhoe Park, Colchester CO4 3SQ, United Kingdom, the [§]Department of Chemistry, University of York, Heslington, York YO10 5DD, United Kingdom, and the [¶]Molecular Biotechnology, Institute of Biology, Sylvius Laboratory, Leiden University, P. O. Box 9505, 2300RA Leiden, The Netherlands

Copper-dependent lytic polysaccharide monooxygenases (LPMOs) are enzymes that oxidatively deconstruct polysaccharides. The active site copper in LPMOs is coordinated by a histidine-brace. This utilizes the amino group and side chain of the N-terminal His residue with the side chain of a second His residue to create a T-shaped arrangement of nitrogen ligands. We report a structural, kinetic, and thermodynamic appraisal of copper binding to the histidine-brace in an auxiliary activity family 10 (AA10) LPMO from *Streptomyces lividans* (*Sli*LPMO10E). Unexpectedly, we discovered the existence of two apo-*Sli*LPMO10E species in solution that can each bind copper at a single site with distinct kinetic and thermodynamic (exothermic and endothermic) properties. The experimental EPR spectrum of copper-bound *Sli*LPMO10E requires the simulation of two different line shapes, implying two different copper-bound species, indicative of three and two nitrogen ligands coordinating the copper. Amino group coordination was probed through the creation of an N-terminal extension variant (*Sli*LPMO10E-Ext). The kinetics and thermodynamics of copper binding to *Sli*LPMO10E-Ext are in accord with copper binding to one of the apo-forms in the wild-type protein, suggesting that amino group coordination is absent in the two-nitrogen coordinate form of *Sli*LPMO10E. Copper binding to *Sli*LPMO10B was also investigated, and again it revealed the presence of two apo-forms with kinetics and stoichiometry of copper binding identical to that of *Sli*LPMO10E. Our findings highlight that heterogeneity exists in the active site copper coordination sphere of LPMOs that may have implications for the mechanism of loading copper in the cell.

Lytic polysaccharide monooxygenases (LPMOs)[3] are enzymes that utilize copper as their functional active site metal and act to enhance the depolymerization of recalcitrant polysaccharides in nature such as cellulose and chitin (1, 2). Identification and characterization of members of this cuproenzyme family from fungal and bacterial species have gathered pace in recent years due in part to their promising uses in biorefinery applications of biomass to derive second generation biofuels (2, 3). LPMOs are classed into auxiliary activity (AA) families in the CAZy (carbohydrate active enzyme) database with four AA families, AA9, AA10, AA11, and AA13 identified so far (4). AA9 (formerly GH61) and AA10 (formerly CBM33) families have been the most extensively studied, with AA9 members having activity for cellulose, hemicellulose, and cellodextrin substrates (5–8) and AA10 members having activity with either cellulose or chitin substrates (9, 10). The AA11 and AA13 families are the most recently discovered, and so far have been determined to have activity with chitin and starch substrates, respectively (11, 12). All LPMOs coordinate a single copper ion by three nitrogen ligands to from the active site. Two of these are provided from the amino group (Nt) and side chain of the N-terminal His with the third from a second His side chain to give a T-shaped copper coordination geometry referred to as the His-brace (6). To initiate enzymatic activity, an electron source is utilized to reduce Cu(II) to Cu(I), with the latter required to activate dioxygen (13, 14). Two principal mechanisms of glycosidic bond cleavage have been proposed (15, 16) with the resulting C1 or C4 oxidation of a sugar ring (6, 8, 15, 17–19) leading to chain breaks that are susceptible to hydrolases for further degradation.

Streptomycetes are the dominant bacterial genus responsible for aerobic biomass decomposition in soil environments and considered vital players in the decomposition of cellulose and other biomass polymers (20–22). Streptomycetes genomes encode a relatively high percentage of genes for putative cellulolytic and chitinolytic enzymes. For example, the secretome of *Streptomyces* sp. SirexAA-E (ActE) has been analyzed through growth on a variety of carbon sources, including cellulose and chitin (23). *Streptomyces coelicolor* and *Streptomyces griseus* have comparable putative genomic compositions of CAZy proteins to ActE; however, these two streptomycetes are less capable of growing on cellulose (23). Thus, not all streptomycetes, despite their abilities to grow on plant polysaccharides (21), are efficient cellulose decomposers.

* The authors declare that they have no conflicts of interest with the contents of this article.

The atomic coordinates and structure factors (code 5ftz) have been deposited in the Protein Data Bank (http://wwpdb.org/).

[1] Recipient of a University of Essex Silberrad Ph.D. scholarship.

[2] To whom correspondence should be addressed. Tel.: 44-1206-872095; E-mail: jworrall@essex.ac.uk.

[3] The abbreviations used are: LPMO, lytic polysaccharide monooxygenase; AA, auxiliary activity; BisTris, 2-[bis(2-hydroxyethyl)amino]-2-(hydroxymethyl)propane-1,3-diol; ITC, isothermal titration calorimetry; Nt, N-terminal amino group.

In liquid-grown cultures, the growth of many streptomycetes is characterized by the formation of large biofilm-like aggregates, called pellets (24, 25). The competence of streptomycetes to directly secrete enzymes into the culture broth makes them attractive hosts for the heterologous production of commercially valuable enzymes (26, 27). However, the pellets suffer from poor efficiency in oxygen and nutrient uptake and thus compromise the overall efficiency of the fermentation process. The synthesis of extracytoplasmic glycans is important for pellet formation (28–31). In *Streptomyces lividans* enzymes encoded by the *cslA-glxA* locus produce a β-(1,4)-glycan at the hyphal tip, of which the chemical composition is unknown (28–30). CslA belongs to the glycosyltransferase family 2, which includes cellulose and chitin synthases, among others (32). Deletion of *cslA* abolishes pellet formation in liquid-grown cultures and also blocks the formation of reproductive aerial hyphae on solid medium (28, 29). GlxA is a newly characterized member of the AA5 family of mono-copper oxidase possessing a Tyr-Cys cross-linked redox cofactor (30). A *glxA* null mutant blocks development and abolishes pellet formation coinciding with the loss of glycan deposition at hyphal tips, the same phenotype as observed with the *cslA* deletion (30, 33). This is consistent with a model whereby CslA and GlxA cooperatively function in glycan deposition at the hyphal tip and are jointly responsible for the formation of reproductive aerial structures and, in liquid environments, for the formation of pellets (30).

Recent studies in *S. lividans* have identified an extracellular copper-trafficking pathway involving two copper chaperone proteins (Sco and ECuC) (34, 35) and a DyP-type heme peroxidase (DtpA) (36) that are all required to facilitate GlxA maturation (*i.e.* copper-loading and subsequent Tyr-Cys cross-link formation (30)). Based on these studies, a model has been developed that proposes the presence of a large protein complex at the hyphal tip for synthesis and deposition of the glycan required for morphogenesis (36). Downstream of *glxA* is the *cslZ* gene, encoding for an endoglucanase, and upstream of *cslA* is a gene (*SLI3182*) predicted to encode for an AA10 LPMO. The *S. lividans* genome has seven genes encoding putative AA10s (*Sli*LPMO10A-G) (37). RNA-sequence data of *S. lividans* grown in a mannitol/glucose media reveal two *slilpmo10* transcripts to be constitutively expressed (*slilpmo10B* and *slilpmo10E*), although the remaining five may be under transcriptional control of a repressor or activator and depend upon induction by a polysaccharide substrate (Table 1).

In this study, we have set out to establish the biochemical and structural properties of *Sli*LPMO10E along with investigating the kinetic and thermodynamic properties of Cu(II) binding to the His-brace. Interestingly, our data are consistent with the His-brace of apo-*Sli*LPMO10E existing in two non-equilibrating forms that can coordinate Cu(II) by three or two nitrogen ligands. Mixed Cu(II) complexes of equal stoichiometry are also inferred from EPR spectral simulations, with the parameters derived indicating that AA10s may not be as rhombic as originally thought but rather reflect a mixture of Cu(II) species.

TABLE 1

Transcription analysis of the seven *lpmo* genes in *S. lividans*

RNA sequence data obtained and reported earlier in liquid minimal media and glucose/mannitol as a carbon source (61) were analyzed with the *S. lividans* 1326 genome sequence as input (37).

Gene	Protein	*S. lividans* 1326[a] (RPKM)[b]	*S. lividans* 1326 + Cu[a] (RPKM)[b]
SLI0440	*Sli*LPMO10A	0	0
SLI0614	*Sli*LPMO10B	10	9
SLI1466	*Sli*LPMO10C	0	6
SLI2039	*Sli*LPMO10D	0	2
SLI3182	*Sli*LPMO10E	22	27
SLI6742	*Sli*LPMO10F	0	0
SLI7441	*Sli*LPMO10G	0	3

[a] The transcriptomes of WT *S. lividans* 1326 were obtained without addition of copper to the growth medium. The copper-induced transcriptome was obtained after a 2-h exposure to 400 μM Cu(II).

[b] The selected expression measure is the RPKM and is defined as the reads/kb of exon/million mapped reads, *i.e.* dividing the total number of exon reads (in this case one exon per reference sequence) by the number of mapped reads (in millions) times the exon length (in kb) (62).

Experimental Procedures

Cloning of LPMOs and Site-directed Mutagenesis—A pET26b plasmid (Novagen) was modified by QuikChange mutagenesis to relocate the NcoI site 6 nucleotides downstream. This modification enabled the overexpression of mature LPMOs correctly processed at the N-terminal His residue following cleavage of the *pelB*-leader sequence. *SLI3182* (nucleotides 88–606) encoding for *Sli*LPMO10E and *SLI0614* (nucleotides 127–687) encoding for *Sli*LPMO10B were amplified from *S. lividans* 1326 and cloned into the modified pET26b plasmid using the new NcoI and original HindIII restriction sites. Site-directed mutagenesis of His-187 to an Ala in *Sli*LPMO10E was carried out by PCR using the wild-type (WT) construct with forward and reverse primers containing the desired nucleotide change. The N-terminal *Sli*LPMO10E extension variant (*Sli*LPMO10E-Ext) whereby His-30 is no longer the N-terminal residue was created by introducing a Gly residue prior to His-30 and cloning into an unmodified pET26b plasmid to give a mature protein with an N-terminal sequence of Met-Gly-His. All constructs were DNA sequenced to corroborate the mutations and insertions.

Overexpression and Purification of LPMOs—All proteins were overexpressed in *Escherichia coli* BL21 (RIL) cells starting from 37 °C overnight pre-cultures that were used to inoculate 500 ml of LB cultures in 2-liter flasks (37 °C, 180 rpm). At an A_{600} of 0.4, the temperature was lowered to 16 °C and isopropyl β-D-1-thiogalactopyranoside (Melford) was added to a final concentration of 1 mM on reaching an A_{600} of 0.6. Cells were harvested after 16 h at 3,501 × *g* for 20 min at 4 °C. Cell pellets were combined, weighed, and resuspended in 1/30th of the total culture volume in ice-cold 50 mM Tris/HCl, pH 8.0, 1 mM EDTA, and 20% w/v sucrose and stirred at 4 °C for 1 h. For every gram of cell pellet, 60 μl of 1 M $MgSO_4$ was added, and stirring was continued for a further 30 min at 4 °C. The smooth cell suspension was then centrifuged at 38,724 × *g* for 20 min at 4 °C, and the supernatant was removed and stored at 4 °C. The pellet was then resuspended in ice-cold water (1/30th the volume of the culture), stirred at 4 °C for 1 h, followed by centrifugation at 38,724 × *g* for 20 min, with the supernatant collected and combined with that from the previous sucrose fractionation. The combined supernatants were then dialyzed overnight against 5 mM Tris/HCl, pH 7, 1 mM EDTA at 4 °C. For *Sli*LPMO10E (pI 8.42) and variants, the dialysate was diluted with buffer A (5 mM Tris/HCl, pH 7) and loaded to a 5-ml

HiTrap SP-column (GE Healthcare) equilibrated with buffer A and eluted with a linear salt gradient using buffer A containing 1 M NaCl. For *Sli*LPMO10B (pI 4.24), the dialysate was diluted with buffer B (10 mM Tris/HCl, pH 5.5) and loaded to a pre-equilibrated DEAE column (GE Healthcare) and eluted with a linear salt gradient using buffer B containing 500 mM NaCl. Fractions containing LPMO were pooled and concentrated at 4 °C using a 5-kDa cutoff Centricon (Vivaspin). Concentrated protein was then loaded to a HiLoad 26/60 Superdex-75 column (GE Healthcare) equilibrated with buffer C (10 mM sodium acetate, pH 5, 150 mM NaCl). Fractions eluting from the major peak were concentrated and used in subsequent experiments.

LPMO Preparation—Protein concentrations were determined by UV-visible spectroscopy on a Varian Cary50 UV-visible spectrophotometer using an extinction coefficient (ϵ) at 280 nm of 36,690 M^{-1} cm^{-1} for *Sli*LPMO10E, H187A, and *Sli*LPMO10E-Ext and 63,160 M^{-1} cm^{-1} for *Sli*LPMO10B (38). Prior to experiments requiring the addition of Cu(II) salts, proteins were incubated for prolonged periods with excess EDTA followed by gel filtration. For Cu(II) titrations and preparation of Cu(II)-loaded enzyme, a stock solution of 100 mM Cu(II)SO_4 (Sigma) was prepared and diluted as required. Cu(II)-loaded enzymes were prepared by stoichiometric addition of Cu(II)SO_4 followed by desalting to ensure no unbound metal remained.

Substrate Binding Assay—*Sli*LPMO10E (~20 μM in 50 μl of 50 mM BisTris/HCl, pH 6.2) was incubated with ~5–10 mg of excess substrate, cellulose (Whatman No. 1, 50 μm), or squid pen β-chitin at room temperature for 3–4 h with occasional agitation. The supernatant was then removed by centrifugation and kept as the unbound fraction. Substrate was then washed three times to remove any unspecific enzyme. Bound enzyme was removed by adding 50 μl of SDS-PAGE loading buffer containing DTT and heating at 95 °C for 10 min. Samples were then analyzed for bound and unbound enzyme content using a 15% SDS-polyacrylamide gel (Bio-Rad).

Mass Spectrometry—Oxidative activity was assayed by mass spectrometry (MS) using a range of substrates (squid pen β-chitin, Avicel (cellulose), Konjac glucomannan, Guar gum, Ivory nut mannan, and Locust bean gum). Reaction mixtures (1 ml total volume) contained 0.2% w/v solid substrate in 10 mM ammonium acetate, pH 5, 1 mM ascorbic acid, and 10 μM copper-loaded LPMO. Control samples were also prepared in the absence of ascorbic acid and protein. Reactions were incubated at 30 °C rotating for 5–12 h before the remaining solid substrate was removed by centrifugation at 16,000 × *g* at 4 °C for 5 min, and the supernatant was used for analysis. 1 μl of sample was mixed with an equal volume of 10 mg/ml 2,5-dihydroxybenzoic acid in 50% acetonitrile, 0.1% trifluoroacetic acid on a SCOUT-MTP 384 target plate (Bruker). The spotted samples were then dried in a vacuum desiccator before being analyzed on an Ultraflex III matrix-assisted laser desorption ionization-time of flight/time of flight (MALDI-TOF/TOF) instrument (Bruker), as described previously (9).

Electron Paramagnetic Resonance (EPR) Spectroscopy and Spectral Simulations—Samples (80 μM) for EPR analysis were prepared in duplicate in 5 mM Tris/HCl, pH 7, 150 mM NaCl with additions of 0.9 eq of Cu(II)SO_4. Wilmad SQ EPR tubes (Wilmad Glass, Buena, NJ) were filled with 250 μl of LPMO solutions, frozen in methanol kept on dry ice, and then transferred to liquid nitrogen. All EPR spectra were measured at 10 K on a Bruker EMX EPR spectrometer (X band). A spherical high quality Bruker resonator ER 4122 SP 9703 and an Oxford Instruments liquid helium system were used to measure the low temperature EPR spectra. Blank spectra of frozen water samples were subtracted from the EPR spectra of the protein samples to eliminate the baseline caused by the resonator's walls, quartz insert, or quartz EPR tube. The baseline was corrected by subtracting a polynomial line drawn through a set of points randomly chosen on the baseline using WinEPR (version 2.22, Bruker Analytik, GmbH). Spectral simulations were performed in SimFonia version 1.26 (Bruker Analytik, GmbH). The g_z value and its hyperfine splitting constant A_z^{Cu} were determined directly from the spectra. Rather than varying g_x and g_y independently, two other values, g_{av} and Δg, were varied, where $g_{av} = (g_x + g_y)/2$ and $\Delta g = g_y - g_{av} = g_{av} - g_x$. To maintain consistency in the simulation procedure while varying the minimal number of parameters, a number of constraints were imposed on the choice of the other simulation parameters thus minimizing the number of varied parameters. Thus, the tensor for the hyperfine interaction of the spin density with copper nucleus A^{Cu} ($I_{Cu} = 3/2$) was assumed axial, with the $A_x^{Cu} = A_y^{Cu} = 0.1\ A_z^{Cu}$ (small variations around empirically picked factor of 0.1 were found to produce a minimal effect on the simulated spectra). Furthermore, all A^{Cu} tensors were assumed co-linear with the *g*-tensor (all Euler angles were assumed zero). Cu(II) coordinating nitrogen atoms ($I_N = 1$) were assumed to produce isotropic hyperfine interactions ($A_x^N = A_y^N = A_z^N = 14$ G). In accordance with earlier reported relationship between principal *g*-factor components and individual line width values along those directions (39), the *x*, *y*, and *z* components of the spectra line width ΔH were assumed to have a close to linear dependence on the *g* values, the higher the g_i, the higher the ΔH_i value. This dependence was maintained for all simulations.

Fluorescence Spectroscopy—Fluorescence spectroscopy was carried out at 20 °C on an LS 50B fluorimeter (PerkinElmer Life Sciences) with emission spectra collected between 300 and 400 nm following excitation at 295 nm. The excitation emission slit widths were both set at 5 nm. LPMO proteins (2 μM) were prepared in 10 mM sodium acetate, pH 5, 150 mM NaCl and titrated with microliter aliquots of a Cu(II)SO_4 solution.

Stopped-flow Kinetics—Kinetic experiments to measure fluorescence emission changes on Cu(II) binding were carried out on a SX20 stopped-flow spectrophotometer (Applied Photophysics) thermostatted at 25 °C. Trp residues were excited at 295 nm and emitted fluorescence sampled at right angles to the exciting beam after passage through a cutoff filter permitting light with wavelengths above 350 nm to pass, thus removing any scattered exciting light. All LPMO samples (2.5 or 5 μM after mixing) were prepared in 10 mM sodium acetate, pH 5, 150 mM NaCl and were rapidly mixed with a range of Cu(II)SO_4 concentrations (25–500 μM after mixing). Following excitation at 295 nm, time courses were taken collecting the total fluorescence emission. Stoichiometry of Cu(II) binding to the LPMOs was monitored by fluorescence amplitude changes. All kinetic

data were analyzed using the ProKinetist software (Applied Photophysics).

Isothermal Titration Calorimetry (ITC)—Calorimetric titration experiments were carried out at 25 ± 0.1 °C on a MicroCal VP-ITC calorimeter in (10 mM sodium acetate, pH 5, 150 mM NaCl). Before each run, samples were degassed for 15 min at 23 ± 0.1 °C using the ThermoVac accessory. A solution of Cu(II)SO_4 (1 mM) was loaded into the injection syringe and titrated into 100 μM WT or variant *Sli*LPMO10E in the sample cell with stirring at 307 rpm for the duration of the experiment. A reference power of 5 μcal/s was used with either an initial 3- or 5-μl injection of Cu(II)SO_4 followed by either a 5- or 10-μl injection for all subsequent titration points. A 60-s initial equilibrium delay with 270-s pauses between subsequent injections were applied throughout. Raw data were analyzed using Origin 7.0 software. The integrated data were corrected for the heat of dilution of buffer into buffer and Cu(II)SO_4 into buffer, and the binding isotherms were fitted using binding models provided in the software package.

Crystallization and Structure Determination—An ARI-Gryphon 96-well crystallization robot was used to screen crystallization conditions for *Sli*LPMO10E. A crystal hit was found in 0.1 M sodium acetate, pH 4.6, 25% PEG 4,000 (PEG suite, Qiagen). Scaling-up and optimization of *Sli*LPMO10E crystals from the initial hit were carried out in 24-well VDX plates (Molecular Dimensions) using the hanging drop vapor diffusion method at 18 °C. Equal volumes of protein (15 mg ml^{-1}) and reservoir solution were mixed, and crystals suitable for diffraction studies grew within 2–3 weeks. A single crystal grown from 0.05 M sodium acetate, pH 4.6, 25% PEG 4,000 was transferred to a cryoprotectant solution containing the respective reservoir solution and 20% glycerol prior to flash-cooling by plunging into liquid nitrogen. Crystallographic data were measured at beamline I03, Diamond Light Source, using an x-ray wavelength of 1.00 Å and a Pilatus 6 M-F detector (Dectris). Data were processed automatically using XDS (40) in XIA2 (41) and scaled and merged using Pointless/Scala (42) in the CCP4i suite. The structure was solved using automated molecular replacement in BALBES with an initial model built-in ArpWarp (43, 44). The structure was refined using Refmac5 (45), with model building between refinement cycles in Coot (46). Riding hydrogen atoms were added when refinement of the protein atoms had converged. Structures were validated using the MolProbity server (47), the JCSG Quality Control Server, and tools within Coot (46). Coordinates and structure factors were deposited in the RCSB Protein Data Bank. A summary of data, refinement statistics, and the quality indicators for the structure are given in Table 2. Additional datasets were collected at wavelengths of 1.20 and 1.33 Å to generate anomalous maps for validation of modeled copper atoms in the structure (Table 2).

TABLE 2

Crystallographic data processing and refinement statistics

Values in parentheses refer to the outermost resolution shells (1.40–1.38, 2.07–2.02, and 2.07–2.01 Å, respectively). The unit cell was $a = 69.6$, $b = 32.4$, $c = 61.3$ Å, $\beta = 97.8°$ in space group C2. R.M.S.D. is root mean square deviation. ESU is estimated standard uncertainty; ML is maximum likelihood.

Wavelength (Å)	1.0	1.33	1.20
Resolution (Å)	1.38	2.02	2.01
Unique reflections	27360	8755	8844
Completeness (%)	97.3 (92.2)	97.6 (90.6)	96.7 (87.2)
R_{merge}	0.055 (0.680)	0.060 (0.087)	0.049 (0.084)
Mn(I/S.D.)	14.8 (1.8)	20.3 (13.7)	24.1 (15.9)
Redundancy	4.9 (3.5)	5.5 (4.7)	5.5 (4.7)
Wilson B-factor (Å^2)	9.3	8.3	9.8
R_{cryst}	0.135		
R_{free}	0.160		
ESU based on ML (Å)	0.038		
R.M.S.D. bond lengths (Å)	0.017		
R.M.S.D. bond angles (°)	1.72		
Ramachandran favored (%)	98.8		
Protein Data Bank code	5ftz		

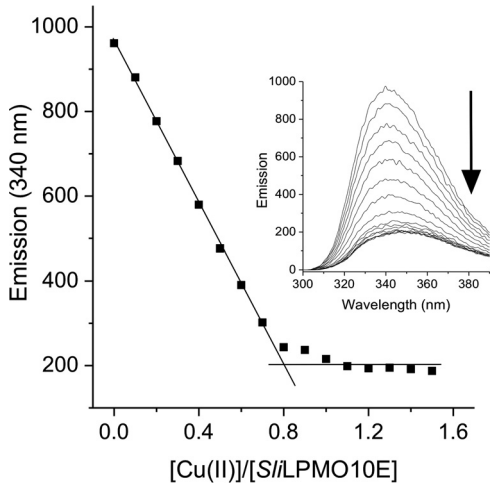

FIGURE 1. **Cu(II) binding to *Sli*LPMO10E at pH 5 and 20 °C.** Changes in the Trp emission spectrum (*inset*) upon titration of 1 mM Cu(II)SO_4 to *Sli*LPMO10E (2 μM) and plotted as a function of [Cu(II)]/[*Sli*LPMO10E] are shown. The *arrow* indicates the direction of the emission change, and the stoichiometry of the reaction is indicated by the intersection of the *two solid lines*.

Results

Trp Fluorescence of Apo-SliLPMO10E Is Quenched upon Binding Cu(II)—Size-exclusion chromatography revealed *Sli*LPMO10E to be a monomeric species, which migrated as a single band on an SDS-polyacrylamide gel to a mass of ~18 kDa (predicted mass 18,422 Da for residues 30–201). Samples of as-purified *Sli*LPMO10E were subjected to ICP-MS analysis, and a copper content of <3% (0.03 μg of atoms/liter) was consistently determined, indicating a predominantly apo-form. Titrating Cu(II) into apo-*Sli*LPMO10E resulted in the quenching of the Trp fluorescence at λ 340 nm (Fig. 1), with a break point reached at ~0.8 to 0.9 eq of copper, indicating a binding stoichiometry close to 1:1 (Fig. 1).

X-band EPR Spectroscopy Infers the Existence of Two Cu(II) Complexes—Apo-*Sli*LPMO10E gave a very weak EPR signal consistent with the presence in the sample of a small amount of Cu(II), in agreement with ICP-MS analysis (Fig. 2*A*). On preparation of holo-*Sli*LPMO10E, a much stronger EPR signal clearly originating from Cu(II) centers is obtained (Fig. 2*B*). Attempts to simulate this experimental spectrum as a single Cu(II) species proved unsuccessful. However, a simulation was possible if a linear combination of two different line shapes was assumed (Fig. 2*C*) with the simulation parameters reported in Table 3. Thus, the experimental EPR spectrum recorded at 10 K for *Sli*LPMO10E is best approximated by a superposition of two different EPR lines, further referred to as Sim1 and Sim2, from two different Cu(II) complexes. Sim1 was simulated for three

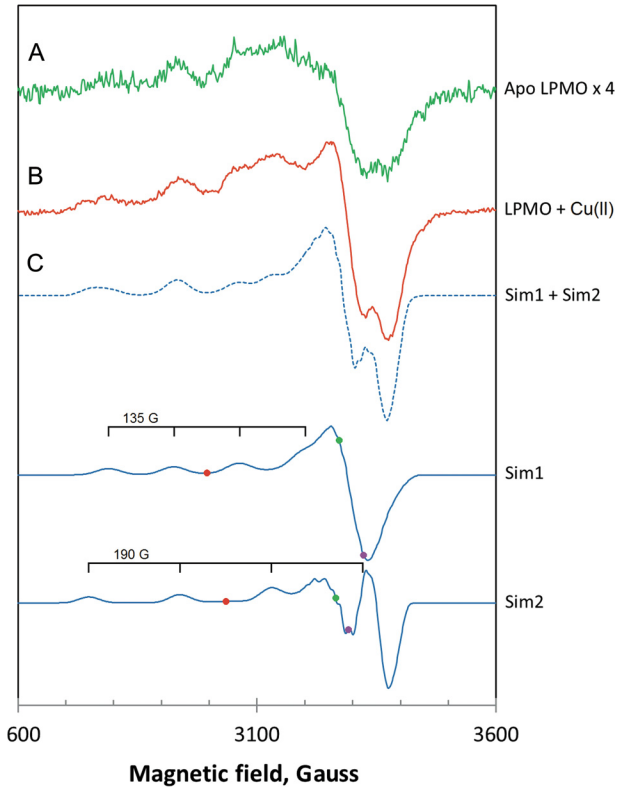

FIGURE 2. **EPR spectra of *Sli*LPMO10E at pH 7 and 10 K.** *A,* as purified magnified ×4, and *B,* loaded with 0.9 eq of Cu(II). The experimental spectrum in *B* (*solid line*) has been approximated by a linear combination (*dotted line*) of the simulated EPR signals Sim1 and Sim2. *C,* simulated EPR spectra of the Cu(II) ion coordinated by three nitrogen ligands (Sim1) and by two nitrogen ligands (Sim2). The *colored dots* on the two simulated spectra indicate the positions of the principal *g*-values used in the simulations, *purple*, g_x; *green*, g_y; *red*, g_z. Each simulated spectrum is labeled with the equidistant *quartet tick marks*, centered at g_z and showing the positions of lines originated from the hyperfine interaction of the Cu(II) electron spin (**S** = 1/2) with the copper nuclear spin (I = 3/2). The simulation parameters are given in Table 3.

TABLE 3

EPR simulation parameters of *Sli*LPMO10E used to simulate spectra Sim1 and Sim2 in Fig. 2

	g	A^{Cu}	A^{N}	ΔH
		G	*G*	*G*
Sim1[a]				
x	2.033	13.5	14	12
y	2.067	13.5	14	13
z	2.260	135	14	26
Sim2[b]				
x	2.055	19	14	12
y	2.071	19	14	13
z	2.230	190	14	23

[a] Data were simulated for three coordinating N atoms.
[b] Data were simulated for two coordinating N atoms.

nitrogen atoms coordinating copper and Sim2 for two nitrogen atoms. One noticeable difference between the line shapes of Sim1 and Sim2 is the presence of a strong "overshoot" line in Sim2. This is a consequence of a combination of two factors as follows: a smaller *g*-factor anisotropy (resulting in a smaller g_z value) and a larger A_z^{Cu} value in Sim2 than in Sim1 (Table 3). The second integrals of Sim1 and Sim2 are similar within 2% accuracy indicating the two Cu(II) complexes are likely to be present in roughly equal concentrations.

SliLPMO10E Has Enzymatic Activity with β-Chitin—Initial substrate binding experiments using cellulose and β-chitin were monitored by SDS-PAGE. *Sli*LPMO10E displayed a clear preference for β-chitin based on the proportion of unbound relative to bound fraction observed on the gel (Fig. 3, *inset*). Substrate specificity and activity were further probed by incubation with diverse glycan substrates (see "Experimental Procedures") in the presence of ascorbate as the reducing agent. MALDI-TOF MS analysis of the reaction products revealed LPMO activity only for β-chitin (Fig. 3). The observed activity was mainly consistent with previous studies on chitin-active AA10s (9), producing predominantly reducing-end aldonic acid oligosaccharide products (C1 oxidation) with even-numbered degrees of polymerization. However, not consistent was the observation of −2 Da species implicated as possible reducing end lactones prior to ring opening or non-reducing end ketoaldoses resulting from C4 oxidation (Fig. 3). Distinguishing these species by MS is challenging, and so from the present data it is unclear whether *Sli*LPMO10E is capable of oxidizing at the C4 as well as the C1 position.

X-ray Crystal Structure of SliLPMO10E Reveals Two Copper-binding Sites—The x-ray structure of holo-*Sli*LPMO10E was determined to a resolution of 1.38 Å and contains one protein molecule in the crystallographic asymmetric unit. Continuous and well defined electron density was found for residues 30–201. The overall structure includes seven anti-parallel β-strands arranged in two β-sheets (Fig. 4*A*); one contains three antiparallel strands (S1, S3, and S6), and the other contains four antiparallel strands (S4, S5, S7, and S8). This distorted β-sandwich fold is consistent with that of other AA10 structures (48–52). Between strands S1 and S3 is the loop 2 region, which shows the most variability in size between LPMO families. In *Sli*LPMO10E, this region consists of two α-helices (H1 and H2) and a small β-strand (S2). Two disulfide bonds are also present, Cys-43/Cys-51 and Cys-78/Cys-196, with the latter connecting loop 2 to the C-terminal β-strand (S8) (Fig. 4*A*). Disulfide bonds have been identified in other LPMOs and most likely confer structural stability.

A well defined 16-σ-peak is observed in the σA-weighted $F_o - F_c$ difference map into which a copper ion was modeled with coordination by three equatorial nitrogen ligands; the Nt of His-30 and the Nδ1 and Nϵ2 atoms of His-30 and His-120, respectively (Fig. 4*B*). This results in the T-shaped His-brace coordination geometry, with bond lengths and angles reported in Table 4. A number of residues commonly found in chitin-active AA10s are noted and include Ala-118, suggested to influence the solvent-facing copper site and Phe-193 (Fig. 4*B*) (52). The latter lies with its Cζ atom only 3.6 Å from the active site copper, a feature consistently found in AA10s but replaced by Tyr in the cellulose-active *S. coelicolor Sc*LPMO10B (a homologue to *Sli*LPMO10B) (52). The side chain orientations of Glu-62 and Val-186 in the vicinity of the copper site make a cavity, which is a feature found in other chitin-active AA10s and has been suggested to accommodate oxygen or the acetyl group of an *N*-acetylglucosamine moiety (52).

The putative substrate-binding surface of *Sli*LPMO10E is flat with two small stretches of opposite surface charge, running either side of the positively charged copper ion (Fig. 4*C*). A prominent surface aromatic residue, Trp-56, is located in the

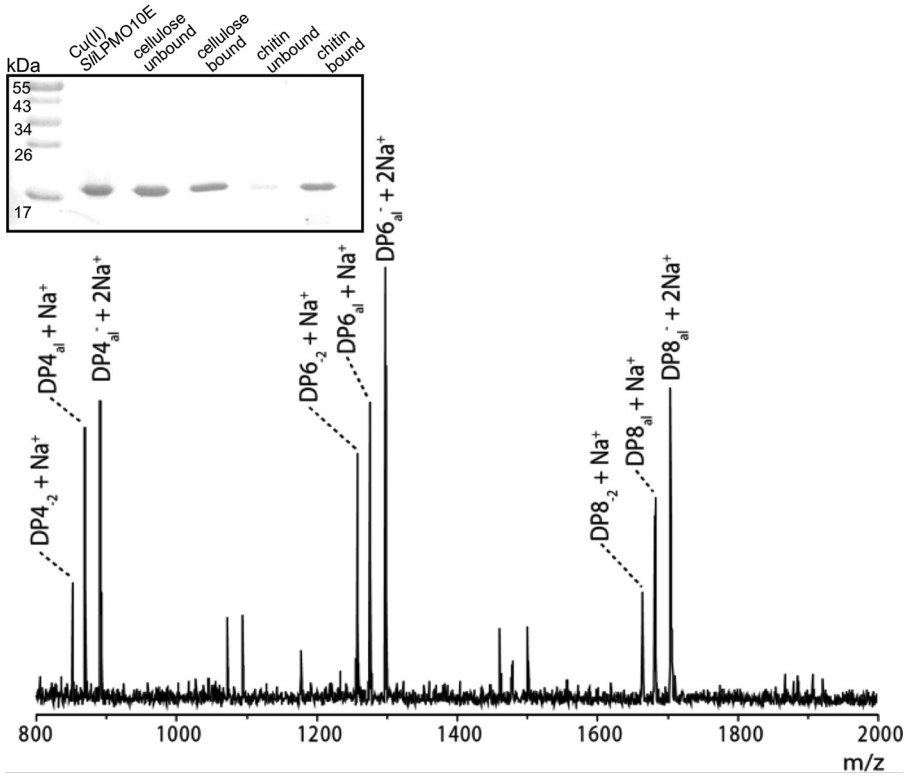

FIGURE 3. **Substrate binding and activity of *Sli*LPMO10E.** *Inset* SDS-PAGE to monitor the binding of *Sli*LPMO10E to cellulose (filter paper) or squid-pen β-chitin. Fractions shown are untreated *Sli*LPMO10E, the protein content in the supernatant (*unbound*) or bound to the substrate (*bound*). MALDI-TOF analysis of *Sli*LPMO10E products from squid-pen β-chitin. DPn_{a1} = aldonic acid; DPn_{-2} = lactone or C4 ketoaldose (measured molecular weight). DP4_{-2} + Na^+ (851.3), DP4_{al} + Na^+ (869.3), DP4_{al}^- + $2Na^+$ (891.3), DP6_{-2} + Na^+ (1257.5), DP6_{al} + Na^+ (1275.5), DP6_{al}^- + $2Na^+$ (1297.5), DP8_{-2} + Na^+ (1663.6), DP8_{al} + Na^+ (1681.7), DP8_{al}^- + $2Na^+$ (1703.6).

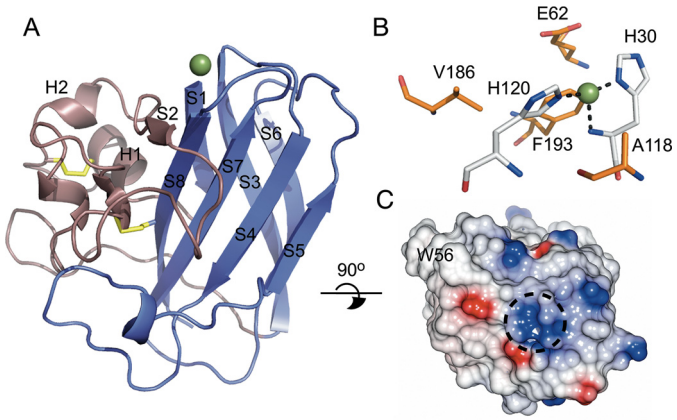

FIGURE 4. **X-ray crystal structure of *Sli*LPMO10E.** *A,* schematic representation with the core β-sheet fold shown in *purple* and the loop 2 region displayed in *violet*. Disulfide bonds are shown in *yellow,* and the copper represented as a *sphere*. *B,* stick representation of the active site. Coordinating His residues are colored in *silver* and residues surrounding the first copper coordination sphere shown in *orange*. Bonds to the copper ion are indicated by *dashed lines*. *C,* electrostatic surface representation of the proposed substrate-binding surface with *W56* labeled and the location of the copper indicated by a *dashed circle*.

TABLE 4
Bond lengths and angles of active site and symmetry-related metal-mediated dimer site (MMD)

Bond	Length/angle (Å, °)
Active site	
His^{30} Nδ1	1.94
His^{30} N	2.24
His^{120} Nϵ2	1.91
His^{30} Nδ1 -Cu- His^{120} N	95
His^{30} Nδ1 -Cu- His^{120} Nϵ2	160
His^{30} N -Cu- His^{120} Nϵ2	103
MMD site	
His^{187} Nϵ2	1.95
Asp^{188} Oδ2	2.40
His^{187} Nϵ2[a]	1.94
Asp^{188} Oδ2[a]	2.42

[a] Symmetry-related molecule is shown.

loop 2 region and is considered important in AA10s for substrate specificity.

A second well defined σ-peak in the σA-weighted $F_o - F_c$ difference map consistent with the presence of a metal ion is also observed. Modeling a copper ion into this peak results in coordination with His-187 and Asp-188 from the monomer in the asymmetric unit and the same residues from a symmetry-related molecule, thus creating a metal-mediated dimer (Fig. 5*A*). Crystallization conditions contained no metal salts, and the excess of Cu(II) used to form the holo-*Sli*LPMO10E was removed prior to crystallization. Although every care was taken to ensure no serendipitous binding of rogue metals, there is the possibility that a divalent metal such as Zn(II) could out-compete Cu(II) for this site. Therefore, to confirm the identity of the metals in both sites (copper or zinc), anomalous difference maps were generated by measuring a single crystal at two different x-ray wavelengths (1.2 and 1.33 Å). At 1.2 Å the energy is above that of both copper and zinc K-edges, whereas at 1.33 Å only the copper K-edge contributes to the anomalous scattering. Anomalous maps generated at these different wavelengths for both the active and dimer sites are consistent with the presence

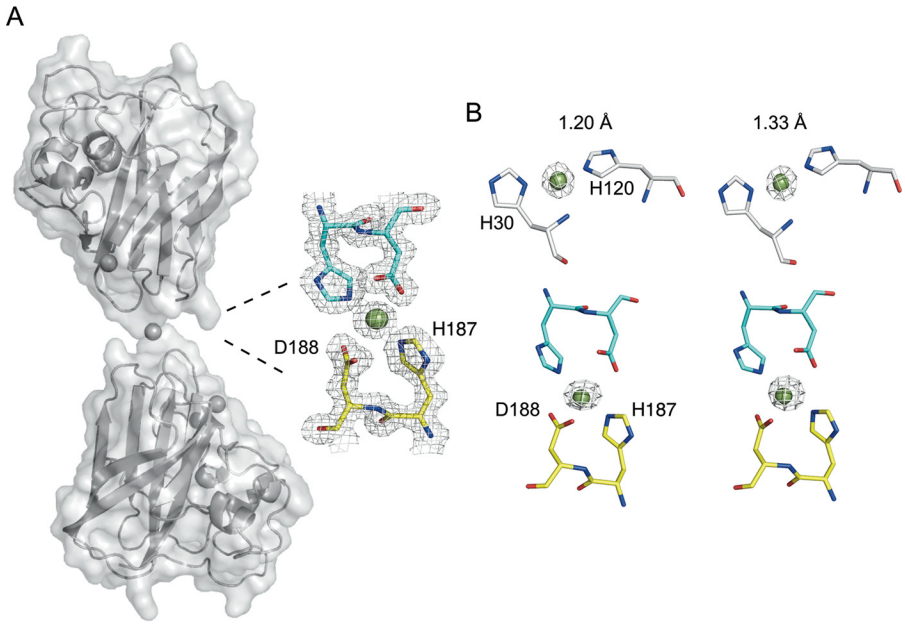

FIGURE 5. **Second metal-binding site creates a metal-mediated *Sli*LPMO10E dimer.** *A,* surface representation of the symmetry-generated metal-mediated dimer of *Sli*LPMO10E together with a $2F_o - F_c$ electron density map contoured at 1 σ of the copper coordination site at the dimer interface. Copper ions are shown in *spheres*. *B,* anomalous electron density maps contoured at 5 σ at x-ray wavelengths of 1.2 Å (above the copper and zinc K-edges) and 1.33 Å (below the zinc but above the copper K-edges) for the active and MMD sites.

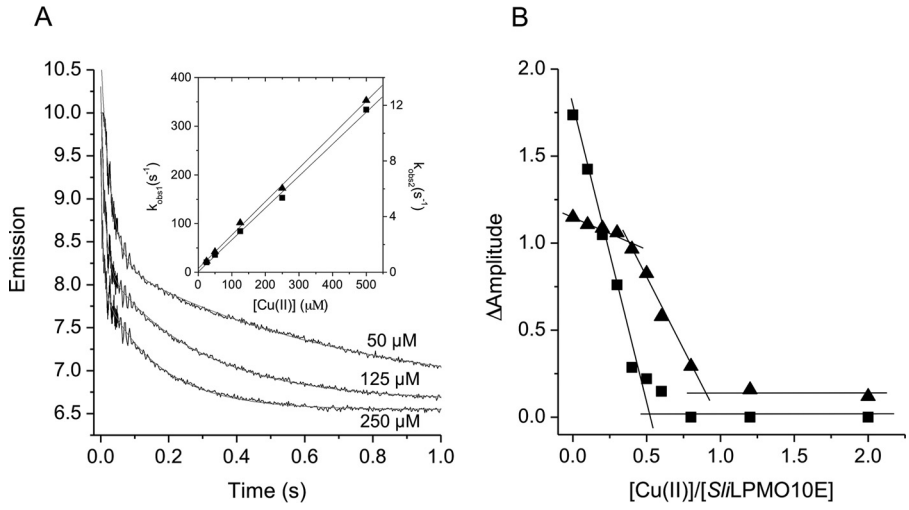

FIGURE 6. **Fluorescence stopped-flow kinetics of Cu(II) binding to *Sli*LPMO10E at pH 5 and 25 °C.** *A,* biphasic time courses and fits to a double exponential function on reacting 2.5 μM (after mixing) *Sli*LPMO10E with various [Cu(II)] as indicated. *Inset,* first-order rate constants for the fast ($k_{obs,\,1}$, *squares*) and the slow ($k_{obs,2}$, *triangles*) phase of Cu(II) binding as a function of [Cu(II)]. *B,* stoichiometry of Cu(II) binding monitored by fluorescence amplitude changes to *Sli*LPMO10E (5 μM after mixing) pre-loaded with sub- to super-stoichiometric amounts of Cu(II), following rapid mixing with excess Cu(II). The fast phase ($k_{obs,\,1}$, *squares*) titrates with an ~0.5 stoichiometry with the slow phase ($k_{obs,\,2}$, *triangles*) being observed following completion of the fast phase and with an ~0.5 stoichiometry.

of a copper ion in both sites (Fig. 5*B*). The copper coordination geometry in the symmetry-generated dimer is a distorted square planar, with the Nϵ2 atoms of the His residues coordinating in a linear fashion and the Oδ2 atoms of the aspartates bent (Table 4). The existence of such a metal-mediated dimer is not readily supported from solution measurements (Fig. 1).

Kinetics of Cu(II) Binding to Apo-SliLPMO10E Reveals Two Binding Forms—Apo-*Sli*LPMO10E was mixed with Cu(II) solutions of known concentrations and the quenching of Trp fluorescence monitored as a function of time in a stopped-flow spectrophotometer. Upon mixing, two phases of fluorescence quenching were observed, the rates of which were [Cu(II)]-dependent (Fig. 6*A, inset*). Pseudo first-order rate constants (k_{obs}) were linearly dependent on the [Cu(II)], with the slopes yielding second-order rate constants, k_1 and k_2 (Fig. 6*A, inset,* and Table 5). The linear plots run through/close to the origin, indicating that the Cu(II) affinity of the binding sites is high (*i.e.* the dissociation rate constants for Cu(II) are small compared with the association rates), and the relative amplitudes of the two phases are independent of the [Cu(II)]. Binding stoichiometries were measured by first loading apo-*Sli*LPMO10E with sub- to super-stoichiometric amounts of Cu(II) followed by mixing with excess Cu(II). Upon mixing, the two phases were retained, but as expected, the total amplitude of the fluorescence quench decreased as the concentration of the Cu(II) preloaded into *Sli*LPMO10E increased (*i.e.* Cu(II) can now only bind to the

TABLE 5

Kinetic and thermodynamic parameters determined from stopped-flow fluorescence, fluorescence titrations, and ITC at 25 °C for Cu(II) binding to the various forms of *Sli*LPMO10E

[a]Fluorescence					
Protein	k_1 ($M^{-1}s^{-1}$)	k_2 ($M^{-1}s^{-1}$)	k_2 (s^{-1})	k_3 (s^{-1})	K_d (M)
*Sli*LPMO10E	6.6 (0.3) x 10^5	2.2 (0.04) x 10^4	-	-	-
H187A	3.6 (0.3) x 10^5	9.2 (0.3) x 10^3	-	-	-
*Sli*LPMO10E -Ext	2.0 (0.2) x 10^6	-	60 (1.7)	0.2 (0.01)	[b]2.4 x 10^{-6} [c]0.5 x 10^{-6}
*Sli*LPMO10B	1.0 (0.1) x 10^6	5.0 (0.2) x 10^4	-	-	-

[d]ITC					
Protein	*N*	K_d (M)	ΔG_b (kcal mol^{-1})	ΔH_b (kcal mol^{-1})	-TΔS (kcal mol^{-1})
[e]*Sli*LPMO10E	0.48 (0.02)	62.5 (0.2) x 10^{-9}	-9.8 (0.3)	-7.9 (0.4)	-1.9 (0.8)
	0.43 (0.05)	4.2 (0.6) x 10^{-6}	-7.3 (0.2)	2.3 (0.5)	-9.6 (0.3)
[e]H187A	0.40 (0.05)	55.8 (2.0) x 10^{-9}	-9.9 (0.8)	-7.9 (0.2)	-2.0 (0.1)
	0.42 (0.1)	4.1 (0.2) x 10^{-6}	-7.4 (0.9)	2.5 (0.4)	-9.9 (0.3)
[f]*Sli*LPMO10E -Ext	0.94 (0.1)	2.6 (0.1) x 10^{-6}	-7.6 (0.5)	20.0 (2.1)	-27.6 (1.1)

[a] Experimental errors are reported in parentheses and are the standard errors from triplicate experiments.
[b] Data were determined from static fluorescence titration.
[c] Data were determined from stopped-flow fluorescence.
[d] Experimental errors are reported in parentheses and are the standard errors from triplicate experiments for *Sli*LPMO10E and duplicates for H187A and *Sli*LPMO10E-EXT.
[e] Parameters were derived from a sequential binding model.
[f] Parameters were derived from a one set of sites binding model.

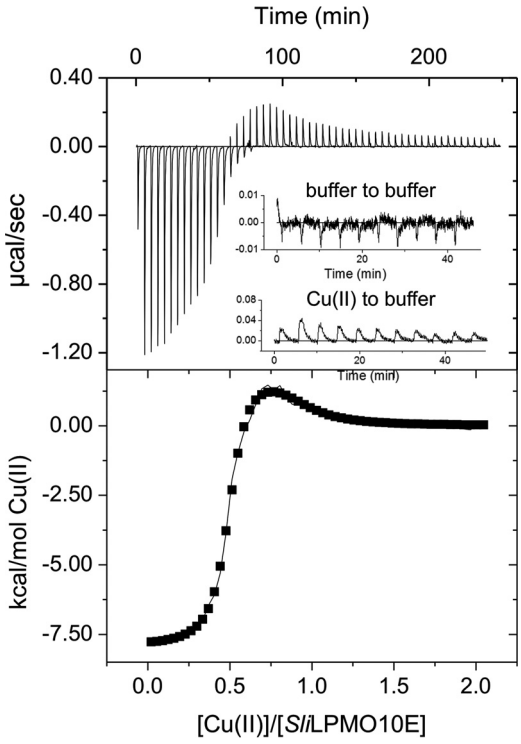

FIGURE 7. **Thermodynamics of Cu(II) binding to *Sli*LPMO10E at pH 5 and 25 °C.** An ITC thermogram and fit to a sequential binding model (*solid line*) upon titrating *Sli*LPMO10E with Cu(II). Thermodynamic parameters obtained are reported in Table 5. *Inset* reports the heat of dilutions from a buffer to buffer and a Cu(II) to buffer titration.

empty sites). The relative amplitudes of the two phases changed as a result of pre-mixing with Cu(II), the faster phase being abolished at lower preloaded Cu(II) additions and the slow phase at higher preloaded [Cu(II)]. This enables the stoichiometry of each phase to be determined as illustrated in Fig. 6*B*. The faster phase titrated with a stoichiometry of ~0.5, and the slower phase, which titrates once the site responsible for the faster binding is filled, also with a stoichiometry of ~0.5. Thus, the overall stoichiometry is 1:1, consistent with the interpretation of the static fluorescence titration (Fig. 1). Furthermore, the proportions of the two kinetic phases are unaffected at low [NaCl]. Therefore the observed [Cu(II)] dependence is not an ionic strength effect, and the data are consistent with Cu(II) binding to two forms of a single site.

The two [Cu(II)]-dependent phases observed in the kinetic measurements prompted us to consider whether the slow phase of Cu(II) binding was due to the presence of a second copper-binding site. Kinetic experiments, with the H187A variant, gave essentially identical results to that of the WT *Sli*LPMO10E, *i.e.* two clear phases both [Cu(II)]-dependent with k_1 and k_2 values reported in Table 5. Thus, the contribution of this dimer site observed in the crystal structure to the quenching of fluorescence in the WT protein may be discounted.

ITC Identifies Two Thermodynamically Distinct Cu(II)-binding Sites—A typical ITC profile obtained by titrating Cu(II) into apo-*Sli*LPMO10E is shown in Fig. 7, where two binding phases are detected. The first of these is an exothermic process with the second endothermic in nature. A two-site model was used to fit the data with the parameters obtained reported in Table 5. Notably, the stoichiometry (*N*) for each binding phase is ~0.5 giving a total stoichiometry of 1 and thus in keeping with the kinetic data. The first binding phase has a nanomolar K_d value for Cu(II) and exhibits a favorable enthalpic binding (ΔH_b) contribution, with a small but favorable entropic ($-T\Delta S$) contribution leading to a favorable free energy of binding (ΔG_b) (Table 5). The second phase displays a weaker affinity for Cu(II) with a micromolar K_d value (Table 5). Moreover, this binding event is characterized by a positive ΔH_b (unfavorable) that is compensated for by an increased $-T\Delta S$, thus maintaining a favorable ΔG_b (Table 5). The H187A mutant gave the same ITC profile with the parameters obtained from fitting to a two-site model comparable with WT *Sli*LPMO10E (Table 5), reconfirming that the second metal site observed in the crystal is not that detected by either kinetics or ITC.

Kinetics of Cu(II) Binding to SliLPMO10B Are Identical to Those of SliLPMO10E—To investigate whether the complex kinetics of Cu(II) binding is unique to *Sli*LPMO10E or may be typical for AA10s, a second AA10 was tested. *Sli*LPMO10B is a homologue of *Sc*LPMO10B from *S. coelicolor* whose structure has been reported and is cellulose-active (52). Size-exclusion chromatography of purified *Sli*LPMO10B revealed a monomer species that migrated as a single band on an SDS-polyacrylamide gel to a mass of ~20 kDa (predicted mass 20,723.4 Da for residues 43–229). Trp fluorescence at $\lambda \geq 350$ nm was quenched upon addition of Cu(II) aliquots, until a break point at ~0.8 to 0.9 eq was reached, indicating a binding stoichiometry close to 1:1. On rapid mixing in the stopped-flow with excess Cu(II), the fluorescence was quenched as seen for

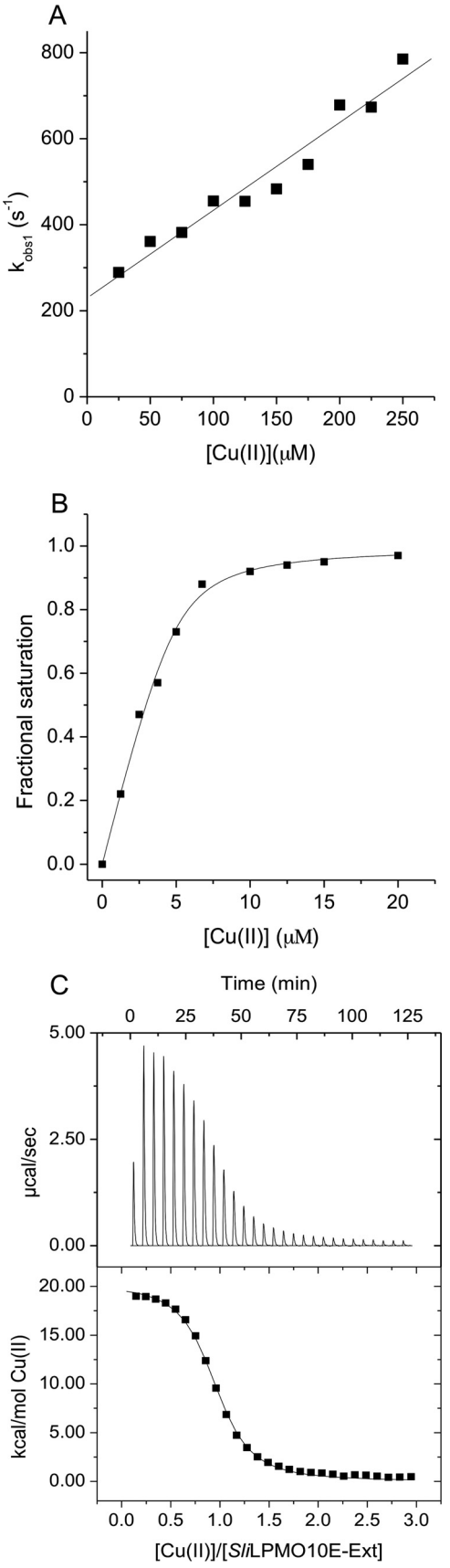

FIGURE 8. **Kinetics and thermodynamics of Cu(II) binding to *Sli*LPMO10E-Ext at pH 5 and 25 °C.** *A*, first-order rate constants for the fast ($k_{obs,\,1}$) phase of Cu(II) binding to *Sli*LPMO10E-Ext as a function of [Cu(II)]. *B*, titration of Cu(II) to *Sli*LPMO10E-Ext plotted as a function of fractional saturation defined as $Y = 1 - \Delta F/\Delta FT$, where ΔF is the fluorescence change and ΔFT is the fluorescent change from zero to fully saturated *Sli*LPMO10E with Cu(II). *C*, ITC binding profile and fit to a single-site binding model (*solid line*) upon titrating *Sli*LPMO10E-Ext with Cu(II). Thermodynamic parameters obtained from the fit are reported in Table 5.

*Sli*LPMO10E with time courses again found to compose two phases, the rate constants of which were linearly dependent on [Cu(II)] (Table 5).

Cu(II) Binding to the SliLPMO10E-Ext Variant Reveals a Single Cu(II) Form—The mature *Sli*LPMO10E-Ext variant has a Met-Gly-His N-terminal sequence and was produced with the aim to abolish/perturb the Nt coordination of the His-brace. *Sli*LPMO10E-Ext remains capable of binding Cu(II) as determined from the quenching of the Trp fluorescence. However, in contrast to *Sli*LPMO10E where the tight binding of Cu(II) precluded the determination of a K_d value (Fig. 1), *Sli*LPMO10E-Ext possesses a weaker affinity for Cu(II) enabling a K_d value to be determined (Table 5). Stopped-flow fluorescence measurements yielded time courses now comprising of three phases after mixing with excess Cu(II). The fastest phase was linearly dependent on [Cu(II)] (Fig. 8*A*) with a second order rate constant (k_1) reported in Table 5. Although binding to this site is rapid, it is with low affinity as seen by the intercept on the $k_{obs,\,1}$ axis, which is interpreted as the dissociation rate constant (k_{off}) of Cu(II) from this site ($k_{off} = 230\ s^{-1}$) (Fig. 8*A*) enabling a K_d of 1.2×10^{-4} M to be determined. The two slower phases display little [Cu(II)] dependence and are assigned to first-order reorganization steps (k_2 and k_3, Table 5) in the Cu(II)-bound *Sli*LPMO10E-Ext that each lead to enhanced quenching of the Trp fluorescence. Titration experiments performed by mixing Cu(II) solutions with *Sli*LPMO10E-Ext preloaded with sub- to super-stoichiometric [Cu(II)] were also carried out. Unlike for *Sli*LPMO10E, the three distinct phases all titrate together indicating binding to a single site that undergoes rearrangement. A striking result is that the K_d value determined following preloading with Cu(II) (Fig. 8*B* and Table 5), is 2 orders of magnitude lower (tighter) than the initial (fast) binding site (K_d 1.2×10^{-4} M) and in line with the K_d value determined from static fluorescence titration experiments (Table 5). Together, these indicate that following initial Cu(II) binding, subsequent rearrangements detected in the slower kinetic phases lock Cu(II) into the site. This is supported by the observed decrease in the amplitude of the slower phase as the [Cu(II)] with which it is mixed increases. This is expected when the [Cu(II)] spans the value of the K_d for the initial binding site. Thus, at 100 μM Cu(II), the amplitude of the fast phase reflects half-occupancy of this site, and full binding then occurs at the rate of the slower phase. At 250 μM Cu(II), ~70% of the initial site is rapidly filled and reflected in the amplitude of the initial binding process, and the remaining sites are filled at the rate of the reorganization.

The ITC profile in Fig. 8*C* shows an endothermic binding event, fitted to a single-site binding model to give the parameters reported in Table 5 for Cu(II) binding to *Sli*LPMO10E-Ext. A stoichiometry of ~1 Cu(II) is determined with a K_d value in the micromolar range correlating well to that determined from the static fluorescence titration and stopped-

flow kinetics (Table 5). The unfavorable ΔH_b is compensated for by a large favorable $-T\Delta S$ contribution, maintaining a favorable ΔG_b (Table 5). Thus, the thermodynamic profile for the *Sli*LPMO10E-Ext variant has a strong resemblance to the second endothermic binding event observed with the WT *Sli*LPMO10E.

Discussion

Two cellulose-degrading AA10s from *S. coelicolor* (*Sc*LPMO10B and *Sc*LPMO10C) and a chitin-degrading AA10 from *S. griseus* (*Sg*LPMO10F) have so far been characterized from streptomycetes (52–54). *Sc*LPMO10C and *Sg*LPMO10F have been shown to oxidize strictly at the C1 carbon of the sugar (52, 54), whereas *Sc*LPMO10B can oxidize at the C1 and C4 positions (52). *Sli*LPMO10E is active only on chitin, with the predominant oxidation product revealed from MS indicative of C1 cleavage (Fig. 3). As described for other AA10s, a Phe and a conserved Ala residue are located in the vicinity of the copper site, with their hydrophobic side chains oriented so as to impede access/binding of exogenous ligands to the axial positions of the copper ion (Fig. 4*B*) (51, 55). This has led to the suggestion that dioxygen activation is most likely at the fourth equatorial position in AA10s resulting in strict C1 substrate oxidation. Conversely, access to the solvent-facing axial position has been suggested to be responsible for C1/C4 oxidation in AA9s lacking an Ala and in *Sc*LPMO10B where the Ala is present but the side chain is positioned so as not to obstruct ligand access (16, 52). In *Sli*LPMO10E, the Ala-118 side chain superimposes with other strict C1-oxidizing AA10s. This structural feature is consistent therefore with the MS interpretation of C1-oxidized products of the chitin substrate and furthermore predicts that the −2 Da species identified in the MS likely arises not from C4 oxidation products but reducing end lactones.

Although a major focus of LPMOs has been on their roles and activities with biomass-derived polysaccharides substrates, the constitutive expression and proximity of *slilpmo10E* to the *cslA-glxA* operon could imply a role in assisting with the attachment or further processing/modification of the *cslA-glxA* glycan produced during the development cycle. The chemical composition of this glycan essential for morphological development in *S. lividans* has not yet been characterized. Typically, genes involved in bacterial cellulose synthesis are organized in an operon, containing the *bcsABCD* genes (56). However, *Streptomyces* lacks a c-di-GMP-binding protein (BcsB), conserved in cellulose-producing organisms and essential for the synthesis of cellulose (57). Therefore, coupled with the activity of *Sli*LPMO10E only for chitin hints at the possibility that the glycan produced by CslA has *N*-acetylglucosamine functionalities.

The x-ray crystal structure of *Sli*LPMO10E reveals the active site copper to have the characteristic His-brace coordination associated with all other LPMOs (Fig. 4). A second coordinating copper ion was also identified in the x-ray structure, with subsequent solution studies providing no evidence to indicate that this second copper site is occupied or that the metal-mediated dimer that can be generated in the crystal is formed. Despite this, the orientation of the two monomers is noteworthy (Fig. 5), as dimerization does not occlude the substrate interaction surface.

Spectral simulation (Sim1 and Sim2) of the EPR spectrum of *Sli*LPMO10E indicates the presence of two Cu(II) species. The g_z and A_z^{Cu} values for these are 2.26/2.23 and 135/190 G, respectively, with the 2.26 and 135 G pair representing the "typical" distorted AA10 coordination where the three nitrogen atoms of the His-brace are all coordinating to the Cu(II). The g_z and A_z^{Cu} values determined directly from the spectral parallel region are the most reliable parameters for comparison with EPR data obtained from other LPMOs. In contrast, the perpendicular g values (g_x and g_y) are estimated through simulation. From this study it is clear that the simulation of spectra for a mixed species gives a significantly lower degree of rhombicity (difference between g_x and g_y) compared with other AA10s (51, 53). Thus previous AA10 values, although recognizant of the difficulty of simulating g_x and g_y values, may reflect a mixture of species rather than true rhombicity (51). For chitin-active AA10s A_z values between 109 and 118 G have been reported (53), placing them between the normal Peisach-Blumberg classification of type 1 and type 2 copper centers (58). In contrast cellulose-active AA10s and AA9s have higher A_z values of ~147 G and are firmly within the type 2 classification (53). Thus *Sli*LPMO10E lies between cellulose-active AA9s/AA10s and chitin-active AA10s, suggesting a more axial geometry compared with other chitin-active AA10s. The second species has a lower g_z value of 2.23 and is in a clearly axial geometry ($A_z = 190$ G). This could arise from a chloride ion binding to the Cu(II), as a consequence of 150 mM NaCl being present in the buffer, in accord with the g_z value of 2.23 recently determined for an AA9 LPMO where chloride acts as the exogenous ligand on Cu(II) (59). The axial geometry may arise from two nitrogen atoms coordinating to the Cu(II), with the decomplexation of one of the His residues or the Nt a possibility, with the coordinated mono-atomic chloride ion able to move around until it overlaps well with the d(x_2-y_2) orbital giving rise to the lower g_z of 2.23 because of enhanced covalency of the singularly occupied molecular orbital across the chloride ligand (59).

In vitro Cu(II) binding studies to *Sli*LPMO10E and *Sli*LPMO10B are most consistent with the mechanism depicted in Fig. 9. Our data suggest that the as-isolated apo-form of these AA10s exist as two non-equilibrating species (*I* and *I**, Fig. 9). Cu(II) first binds to species I in an exothermic reaction with a nanomolar K_d value, which we attribute to Cu(II) coordinating all three nitrogen ligands of the His-brace. Once the Cu(II)-binding site in species I is filled, the second apo-species (I*) binds Cu(II) in an endothermic manner with a micromolar K_d value and is attributed to Cu(II) coordinating two nitrogen ligands of the His brace, with H_2O (low salt conditions) or chloride ions (high salt conditions) completing the equatorial coordination sphere (*X* in Fig. 9). Thus, under the conditions investigated (low and high salt), Cu(II) binds to a single site in two binding forms, each with distinct kinetic and thermodynamic parameters (Fig. 9 and Table 5). Comparison of the kinetic and thermodynamic data for the *Sli*LPMO10E-Ext variant with that of the WT gives a strong indication that the two coordinate nitrogen species arises from the absence of Nt coordination (Fig. 9 and Table 5). This interpretation arises from the unfa-

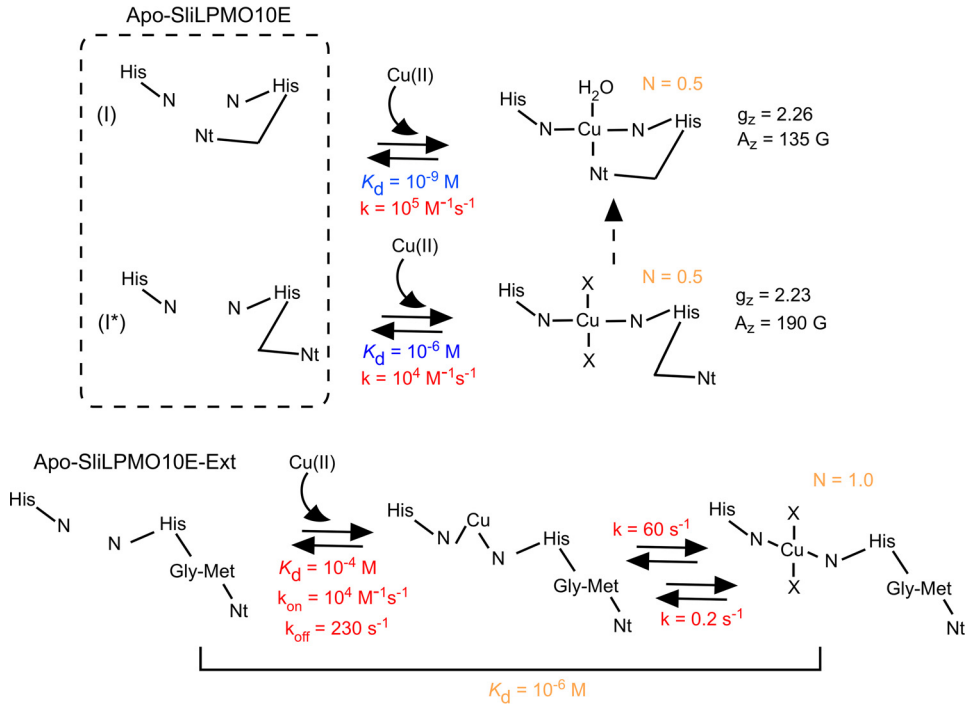

FIGURE 9. **Mechanism of Cu(II) binding to *Sli*LPMO10E and the N-terminal extension variant *Sli*LPMO10E-Ext.** Dissociation constants (K_d) and rates (k) for Cu(II) binding are reported in *blue* (ITC measurement) and *red* (stopped-flow kinetics), with parameters obtained from both experimental approaches given in *orange,* including the stoichiometry of Cu(II) binding (N). The g_z and A_z values determined by EPR for the two Cu(II) species in WT *Sli*LPMO10E are reported. The minimum number of ligands for Cu(II) is four. *X* represents either H_2O or chloride ligand depending on the experimental conditions (*i.e.* high or low NaCl) with chloride more likely under the high NaCl conditions based on the g_z value obtained by EPR.

vorable ΔH_b and K_d values that mirror the second binding form of the WT protein (overall K_d 10^{-6} M) and the presence of a single Cu(II)-dependent binding step (Table 5). The proposition that the kinetics and EPR results arise from two forms of a single site must be set against the structural data that show a single unique copper-binding configuration. One way to account for this apparent discrepancy is by proposing that one of the forms discerned in the kinetic experiments resides at lower energy than the other form. Once Cu(II) is bound, the whole of the protein slowly converts to the lower energy form with the Nt moving inward and completing the three coordinate His-brace geometry as seen in the x-ray crystal structure (*dashed arrow,* Fig. 9). This final conversion would be difficult to detect in fluorescence experiments, as it would occur in the Cu(II)-bound form in which fluorescence is largely quenched.

The fact that we have observed heterogeneity in the His-brace coordination geometry in all batches of *Sli*LPMO10E and *Sli*LPMO10B prepared lends credence to the view that coordination flexibility is inherent in the His-brace motif. The question therefore arises as to what biological function this may be assigned. It is possible that the two forms have different enzymic functions or the flexibility of the copper site is important for loading copper from an *in vivo* donor (*i.e.* chaperone or low molecular weight ligand). In this respect any putative donor will have a very high affinity for copper with the metal only being transferred through docking and orienting the donor and acceptor ligands to enable facile metal transfer through a ligand exchange mechanism (60). Here, we are loading copper in a way that would never happen *in vivo*, namely copper is added in large excess in a non-coordinating form. Therefore, what we may be observing is a heterogeneity of the metal-binding site that in some way reflects different states of the protein, which maybe populated transiently in the true biological transfer. Finally, it is worth considering that these AA10s are Sec substrates and fold following translocation across the membrane. As the protein passes into the extracellular space, copper may become quickly bound (via a chaperone or low molecular weight ligand) prior to cleavage of the signal sequence that then enables for the final nitrogen coordination by the Nt. This is reminiscent of copper binding to the Ext mutant that incorporates the metal into a *single* site, which once having undergone rearrangement binds copper tightly (Fig. 9). If this happens with the signal sequence in place, then cleavage and coordination of the final nitrogen ligand occur when the site is already full. The as-purified WT LPMO proteins lack the signal sequence and in its absence result in two species. These can adopt two folded forms of the His-brace in the apo-state (Nt "out" or "in") that upon *in vitro* copper loading result in the heterogeneity observed, whereas the Ext mutant may replicate the true mechanism of copper binding *in vivo*.

Author Contributions—A. K. C. conducted all experiments, prepared all samples, and analyzed all data. M. T. W. assisted with stopped-flow experiments and analyzed the data. M. A. H. supervised the crystallography and structure determination. D. A. S. carried out EPR experiments and spectral simulations. P. H. W. and G. R. H. contributed reagents, mass spectrometry, and EPR discussion. E. V. carried out RNA-sequence analysis. J. A. R. W. designed the study and wrote the manuscript with contributions from all co-authors.

Acknowledgments—We thank Professor R. Hider for access to ICP-MS measurements at the Institute of Pharmaceutical Science, King's College London. We also thank Dr. Dennis Claessen for critical reading of the manuscript. We acknowledge the Diamond Light Source for access to beamline I03 (East of England Macromolecular Crystallography BAG, MX7461) and use of the JCSG Quality Control Server.

References

1. Beeson, W. T., Vu, V. V., Span, E. A., Phillips, C. M., and Marletta, M. A. (2015) Cellulose degradation by polysaccharide monooxygenases. *Annu. Rev. Biochem.* **84,** 923–946
2. Hemsworth, G. R., Johnston, E. M., Davies, G. J., and Walton, P. H. (2015) Lytic polysaccharide monooxygenases in biomass conversion. *Trends Biotechnol.* **33,** 747–761
3. Müller, G., Várnai, A., Johansen, K. S., Eijsink, V. G., and Horn, S. J. (2015) Harnessing the potential of LPMO-containing cellulase cocktails poses new demands on processing conditions. *Biotechnol. Biofuels* **8,** 187
4. Lombard, V., Golaconda Ramulu, H., Drula, E., Coutinho, P. M., and Henrissat, B. (2014) The carbohydrate-active enzymes database (CAZy) in 2013. *Nucleic Acids Res.* **42,** D490–D495
5. Harris, P. V., Welner, D., McFarland, K. C., Re, E., Navarro Poulsen, J. C., Brown, K., Salbo, R., Ding, H., Vlasenko, E., Merino, S., Xu, F., Cherry, J., Larsen, S., and Lo Leggio, L. (2010) Stimulation of lignocellulosic biomass hydrolysis by proteins of glycoside hydrolase family 61: structure and function of a large, enigmatic family. *Biochemistry* **49,** 3305–3316
6. Quinlan, R. J., Sweeney, M. D., Lo Leggio, L., Otten, H., Poulsen, J. C., Johansen, K. S., Krogh, K. B., Jørgensen, C. I., Tovborg, M., Anthonsen, A., Tryfona, T., Walter, C. P., Dupree, P., Xu, F., Davies, G. J., and Walton, P. H. (2011) Insights into the oxidative degradation of cellulose by a copper metalloenzyme that exploits biomass components. *Proc. Natl. Acad. Sci. U.S.A.* **108,** 15079–15084
7. Agger, J. W., Isaksen, T., Várnai, A., Vidal-Melgosa, S., Willats, W. G., Ludwig, R., Horn, S. J., Eijsink, V. G., and Westereng, B. (2014) Discovery of LPMO activity on hemicelluloses shows the importance of oxidative processes in plant cell wall degradation. *Proc. Natl. Acad. Sci. U.S.A.* **111,** 6287–6292
8. Isaksen, T., Westereng, B., Aachmann, F. L., Agger, J. W., Kracher, D., Kittl, R., Ludwig, R., Haltrich, D., Eijsink, V. G., and Horn, S. J. (2014) A C4-oxidizing lytic polysaccharide monooxygenase cleaving both cellulose and cello-oligosaccharides. *J. Biol. Chem.* **289,** 2632–2642
9. Vaaje-Kolstad, G., Westereng, B., Horn, S. J., Liu, Z., Zhai, H., Sørlie, M., and Eijsink, V. G. (2010) An oxidative enzyme boosting the enzymatic conversion of recalcitrant polysaccharides. *Science* **330,** 219–222
10. Forsberg, Z., Vaaje-Kolstad, G., Westereng, B., Bunæs, A. C., Stenstrøm, Y., MacKenzie, A., Sørlie, M., Horn, S. J., and Eijsink, V. G. (2011) Cleavage of cellulose by a CBM33 protein. *Protein Sci.* **20,** 1479–1483
11. Hemsworth, G. R., Henrissat, B., Davies, G. J., and Walton, P. H. (2014) Discovery and characterization of a new family of lytic polysaccharide monooxygenases. *Nat. Chem. Biol.* **10,** 122–126
12. Lo Leggio, L., Simmons, T. J., Poulsen, J. C., Frandsen, K. E., Hemsworth, G. R., Stringer, M. A., von Freiesleben, P., Tovborg, M., Johansen, K. S., De Maria, L., Harris, P. V., Soong, C. L., Dupree, P., Tryfona, T., Lenfant, N., *et al.* (2015) Structure and boosting activity of a starch-degrading lytic polysaccharide monooxygenase. *Nat. Commun.* **6,** 5961
13. Tan, T. C., Kracher, D., Gandini, R., Sygmund, C., Kittl, R., Haltrich, D., Hällberg, B. M., Ludwig, R., and Divne, C. (2015) Structural basis for cellobiose dehydrogenase action during oxidative cellulose degradation. *Nat. Commun.* **6,** 7542
14. Westereng, B., Cannella, D., Wittrup Agger, J., Jørgensen, H., Larsen Andersen, M., Eijsink, V. G., and Felby, C. (2015) Enzymatic cellulose oxidation is linked to lignin by long-range electron transfer. *Sci. Rep.* **5,** 18561
15. Beeson, W. T., Phillips, C. M., Cate, J. H., and Marletta, M. A. (2012) Oxidative cleavage of cellulose by fungal copper-dependent polysaccharide monooxygenases. *J. Am. Chem. Soc.* **134,** 890–892
16. Kim, S., Ståhlberg, J., Sandgren, M., Paton, R. S., and Beckham, G. T. (2014) Quantum mechanical calculations suggest that lytic polysaccharide monooxygenases use a copper-oxyl, oxygen-rebound mechanism. *Proc. Natl. Acad. Sci. U.S.A.* **111,** 149–154
17. Phillips, C. M., Beeson, W. T., Cate, J. H., and Marletta, M. A. (2011) Cellobiose dehydrogenase and a copper-dependent polysaccharide monooxygenase potentiate cellulose degradation by *Neurospora crassa*. *ACS Chem. Biol.* **6,** 1399–1406
18. Li, X., Beeson, W. T., 4th, Phillips, C. M., Marletta, M. A., and Cate, J. H. (2012) Structural basis for substrate targeting and catalysis by fungal polysaccharide monooxygenases. *Structure* **20,** 1051–1061
19. Vu, V. V., Beeson, W. T., Phillips, C. M., Cate, J. H., and Marletta, M. A. (2014) Determinants of regioselective hydroxylation in the fungal polysaccharide monooxygenases. *J. Am. Chem. Soc.* **136,** 562–565
20. Crawford, D. L. (1978) Lignocellulose decomposition by selected *Streptomyces* strains. *Appl. Environ. Microbiol.* **35,** 1041–1045
21. Goodfellow, M., and Williams, S. T. (1983) Ecology of actinomycetes. *Annu. Rev. Microbiol.* **37,** 189–216
22. McCarthy, A. J., and Williams, S. T. (1992) Actinomycetes as agents of biodegradation in the environment. *Gene* **115,** 189–192
23. Takasuka, T. E., Book, A. J., Lewin, G. R., Currie, C. R., and Fox, B. G. (2013) Aerobic deconstruction of cellulosic biomass by an insect-associated *Streptomyces*. *Sci. Rep.* **3,** 1030
24. Nielsen, J. (1996) Modelling the morphology of filamentous microorganisms. *Trends Biotechnol.* **14,** 438–443
25. van Dissel, D., Claessen, D., and van Wezel, G. P. (2014) Morphogenesis of *Streptomyces* in submerged cultures. *Adv. Appl. Microbiol.* **89,** 1–45
26. Vrancken, K., and Anné, J. (2009) Secretory production of recombinant proteins by *Streptomyces*. *Future Microbiol.* **4,** 181–188
27. Anné, J., Maldonado, B., Van Impe, J., Van Mellaert, L., and Bernaerts, K. (2012) Recombinant protein production and streptomycetes. *J. Biotechnol.* **158,** 159–167
28. Xu, H., Chater, K. F., Deng, Z., and Tao, M. (2008) A cellulose synthase-like protein involved in hyphal tip growth and morphological differentiation in *Streptomyces*. *J. Bacteriol.* **190,** 4971–4978
29. van Veluw, G. J., Petrus, M. L., Gubbens, J., de Graaf, R., de Jong, I. P., van Wezel, G. P., Wösten, H. A., and Claessen, D. (2012) Analysis of two distinct mycelial populations in liquid-grown *Streptomyces* cultures using a flow cytometry-based proteomics approach. *Appl. Microbiol. Biotechnol.* **96,** 1301–1312
30. Chaplin, A. K., Petrus, M. L., Mangiameli, G., Hough, M. A., Svistunenko, D. A., Nicholls, P., Claessen, D., Vijgenboom, E., and Worrall, J. A. (2015) GlxA is a new structural member of the radical copper oxidase family and is required for glycan deposition at hyphal tips and morphogenesis of *Streptomyces lividans*. *Biochem. J.* **469,** 433–444
31. van Dissel, D., Claessen, D., Roth, M., and van Wezel, G. P. (2015) A novel locus for mycelial aggregation forms a gateway to improved *Streptomyces* cell factories. *Microb. Cell Fact.* **14,** 44
32. Cantarel, B. L., Coutinho, P. M., Rancurel, C., Bernard, T., Lombard, V., and Henrissat, B. (2009) The Carbohydrate-Active EnZymes database (CAZy): an expert resource for glycogenomics. *Nucleic Acids Res.* **37,** D233–D238
33. Liman, R., Facey, P. D., van Keulen, G., Dyson, P. J., and Del Sol, R. (2013) A laterally acquired galactose oxidase-like gene is required for aerial development during osmotic stress in *Streptomyces coelicolor*. *PLoS ONE* **8,** e54112
34. Blundell, K. L., Wilson, M. T., Svistunenko, D. A., Vijgenboom, E., and Worrall, J. A. (2013) Morphological development and cytochrome *c* oxidase activity in *Streptomyces lividans* are dependent on the action of a copper bound Sco protein. *Open Biol.* **3,** 20163
35. Blundell, K. L., Hough, M. A., Vijgenboom, E., and Worrall, J. A. (2014) Structural and mechanistic insights into an extracytoplasmic copper trafficking pathway in *Streptomyces lividans*. *Biochem. J.* **459,** 525–538
36. Petrus, M. L., Vijgenboom, E., Chaplin, A. K., Worrall, J. A., van Wezel, G. P., and Claessen, D. (2016) The DyP-type peroxidase DtpA is a Tat-substrate required for GlxA maturation and morphogenesis in *Streptomyces*. *Open Biol.* **6,** 150149
37. Cruz-Morales, P., Vijgenboom, E., Iruegas-Bocardo, F., Girard, G., Yáñez-Guerra, L. A., Ramos-Aboites, H. E., Péronnet, J. L., Anné, J., van Wezel,

G. P., and Barone-Gómez, F. (2013) The genome sequence of *Streptomyces lividans* 66 reveals a novel tRNA-dependent peptide biosynthetic system within a metal-related genomic island. *Genome Biol. Evol.* **5,** 1165–1175
38. Gasteiger, E., Gattiker, A., Hoogland, C., Ivanyi, I., Appel, R. D., and Bairoch, A. (2003) ExPASy: The proteomics server for in-depth protein knowledge and analysis. *Nucleic Acids Res.* **31,** 3784–3788
39. Svistunenko, D. A., and Cooper, C. E. (2004) A new method of identifying the site of tyrosyl radicals in proteins. *Biophys. J.* **87,** 582–595
40. Kabsch, W. (2010) XDS. *Acta Crystallogr. D Biol. Crystallogr.* **66,** 125–132
41. Winter, G. (2010) xia2: an expert system for macromolecular crystallography data reduction. *J. Appl. Crystallogr.* **43,** 186–190
42. Evans, P. R., and Murshudov, G. N. (2013) How good are my data and what is the resolution? *Acta Crystallogr. D Biol. Crystallogr.* **69,** 1204–1214
43. Langer, G., Cohen, S. X., Lamzin, V. S., and Perrakis, A. (2008) Automated macromolecular model building for x-ray crystallography using ARP/wARP version 7. *Nat. Protoc.* **3,** 1171–1179
44. Long, F., Vagin, A. A., Young, P., and Murshudov, G. N. (2008) BALBES: a molecular-replacement pipeline. *Acta Crystallogr. D Biol. Crystallogr.* **64,** 125–132
45. Murshudov, G. N., Vagin, A. A., and Dodson, E. J. (1997) Refinement of macromolecular structures by the maximum-likelihood method. *Acta Crystallogr. D Biol. Crystallogr.* **53,** 240–255
46. Emsley, P., and Cowtan, K. (2004) Coot: model-building tools for molecular graphics. *Acta Crystallogr. D Biol. Crystallogr.* **60,** 2126–2132
47. Davis, I. W., Leaver-Fay, A., Chen, V. B., Block, J. N., Kapral, G. J., Wang, X., Murray, L. W., Arendall, W. B., 3rd, Snoeyink, J., Richardson, J. S., and Richardson, D. C. (2007) MolProbity: all-atom contacts and structure validation for proteins and nucleic acids. *Nucleic Acids Res.* **35,** W375–W383
48. Vaaje-Kolstad, G., Houston, D. R., Riemen, A. H., Eijsink, V. G., and van Aalten, D. M. (2005) Crystal structure and binding properties of the *Serratia marcescens* chitin-binding protein CBP21. *J. Biol. Chem.* **280,** 11313–11319
49. Vaaje-Kolstad, G., Bøhle, L. A., Gåseidnes, S., Dalhus, B., Bjørås, M., Mathiesen, G., and Eijsink, V. G. (2012) Characterization of the chitinolytic machinery of *Enterococcus faecalis* V583 and high-resolution structure of its oxidative CBM33 enzyme. *J. Mol. Biol.* **416,** 239–254
50. Wong, E., Vaaje-Kolstad, G., Ghosh, A., Hurtado-Guerrero, R., Konarev, P. V., Ibrahim, A. F., Svergun, D. I., Eijsink, V. G., Chatterjee, N. S., and van Aalten, D. M. (2012) The *Vibrio cholerae* colonization factor GbpA possesses a modular structure that governs binding to different host surfaces. *PLoS Pathog.* **8,** e1002373
51. Hemsworth, G. R., Taylor, E. J., Kim, R. Q., Gregory, R. C., Lewis, S. J., Turkenburg, J. P., Parkin, A., Davies, G. J., and Walton, P. H. (2013) The copper active site of CBM33 polysaccharide oxygenases. *J. Am. Chem. Soc.* **135,** 6069–6077
52. Forsberg, Z., Mackenzie, A. K., Sørlie, M., Røhr, Å. K., Helland, R., Arvai, A. S., Vaaje-Kolstad, G., and Eijsink, V. G. (2014) Structural and functional characterization of a conserved pair of bacterial cellulose-oxidizing lytic polysaccharide monooxygenases. *Proc. Natl. Acad. Sci. U.S.A.* **111,** 8446–8451
53. Forsberg, Z., Røhr, A. K., Mekasha, S., Andersson, K. K., Eijsink, V. G., Vaaje-Kolstad, G., and Sørlie, M. (2014) Comparative study of two chitin-active and two cellulose-active AA10-type lytic polysaccharide monooxygenases. *Biochemistry* **53,** 1647–1656
54. Nakagawa, Y. S., Kudo, M., Loose, J. S., Ishikawa, T., Totani, K., Eijsink, V. G., and Vaaje-Kolstad, G. (2015) A small lytic polysaccharide monooxygenase from *Streptomyces griseus* targeting α- and β-chitin. *FEBS J.* **282,** 1065–1079
55. Hemsworth, G. R., Davies, G. J., and Walton, P. H. (2013) Recent insights into copper-containing lytic polysaccharide mono-oxygenases. *Curr. Opin. Struct. Biol.* **23,** 660–668
56. Römling, U. (2002) Molecular biology of cellulose production in bacteria. *Res. Microbiol.* **153,** 205–212
57. Ross, P., Mayer, R., and Benziman, M. (1991) Cellulose biosynthesis and function in bacteria. *Microbiol. Rev.* **55,** 35–58
58. Peisach, J., and Blumberg, W. E. (1974) Structural implications derived from the analysis of electron paramagnetic resonance spectra of natural and artificial copper proteins. *Arch. Biochem. Biophys.* **165,** 691–708
59. Frandsen, K. E., Simmons, T. J., Dupree, P., Poulsen, J. C., Hemsworth, G. R., Ciano, L., Johnston, E. M., Tovborg, M., Johansen, K. S., von Freiesleben, P., Mar muse, L., Fort, S., Cottaz, S., Driguez, H., Henrissat, B., *et al.* (2016) The molecular basis of polysaccharide cleavage by lytic polysaccharide. *Nat. Chem. Biol.* **12,** 298–303
60. Banci, L., Bertini, I., Cantini, F., Felli, I. C., Gonnelli, L., Hadjiliadis, N., Pierattelli, R., Rosato, A., and Voulgaris, P. (2006) The Atx1-Ccc2 complex is a metal-mediated protein-protein interaction. *Nat. Chem. Biol.* **2,** 367–368
61. Dwarakanath, S., Chaplin, A. K., Hough, M. A., Rigali, S., Vijgenboom, E., and Worrall, J. A. (2012) Response to copper stress in Streptomyces lividans extends beyond genes under direct control of a copper-sensitive operon repressor protein (CsoR). *J. Biol. Chem.* **287,** 17833–17847
62. Mortazavi, A., Williams, B. A., McCue, K., Schaeffer, L., and Wold, B. (2008) Mapping and quantifying mammalian transcriptomes by RNA-Seq. *Nat. Methods* **5,** 621–628